

(HCN)_m–M_n (M = K, Ca, Sr): Vibrational Excitation Induced Solvation and Desolvation of Dopants in and on Helium Nanodroplets

Gary E. Douberly,^{*,†,‡} Paul L. Stiles,^{†,§} Roger E. Miller,[†] Roman Schmied,^{||,⊥} and Kevin K. Lehmann[¶]

Department of Chemistry, University of North Carolina, Chapel Hill, North Carolina 27599-3290, Department of Chemistry, Princeton University, Princeton, New Jersey 08544, and Department of Chemistry, University of Virginia, Charlottesville, Virginia 22904-4319

Received: September 12, 2009; Revised Manuscript Received: January 29, 2010

Infrared (IR) laser spectroscopy is used to probe the rotational and vibrational dynamics of the (HCN)_m–M_n (M = K, Ca, Sr) complexes, either solvated within or bound to the surface of helium nanodroplets. The IR spectra of the (HCN)_m–K (*m* = 1–3), HCN–Sr, and HCN–Ca complexes have the signature of a *surface* species, similar to the previously reported spectra of HCN–M (M = Na, K, Rb, Cs) [Douberly, G. E.; Miller, R. E. *J. Phys. Chem. A* **2007**, *111*, 7292.]. A second band in the HCN–Ca spectrum is assigned to a *solvated* complex. The relative intensities of the two HCN–Ca bands are droplet size dependent, with the solvated species being favored in larger droplets. IR–IR double resonance spectroscopy is used to probe the interconversion of the two distinct HCN–Ca populations. While only a surface-bound HCN–Sr species is initially produced, CH stretch vibrational excitation results in a population transfer to a solvated state. Complexes containing multiple HCN molecules and one Sr atom are surface-bound, while the ν_1 (HCN)₂Ca spectrum has both the solvated and surface-bound signatures. All HCN–(Ca,Sr)_n (*n* ≥ 2) complexes are solvated following cluster formation in the droplet. Density-functional calculations of helium nanodroplets interacting with the HCN–M show surface binding for M = Na with a binding energy of 95 cm^{–1}. The calculations predict a fully solvated complex for M = Ca. For M = Sr, a 2.2 cm^{–1} barrier is predicted between nearly isoenergetic surface binding and solvated states.

Introduction

As the use of helium droplets as a cold, nanoscale vessel for the investigation of novel, metastable species has expanded,^{1–5} so has the need for a better understanding of the physics that dictate solvation in this exotic environment. There is now a large body of work demonstrating that molecular dopants are solvated within helium droplets.² Atoms can be either solvated or surface bound, and there are two reports of surface bound atom–molecule complexes.^{6,7} In the current report, we take advantage of IR laser spectroscopy to effectively probe the solvation environment of (HCN)_m–M_n (M = K, Ca, Sr) molecular dopants, providing insight into the interactions of these impurities with superfluid helium droplets.

It is now well established that alkali atoms reside in a dimple on the helium droplet surface.⁸ Several high level ab initio calculations of the M–He pair potentials have been reported in an attempt to predict the location of alkali and alkaline earth atoms based on the Ancilloto parameter,⁹ which is a metric for the relative stability of surface and solvated states. The Ancilloto parameters derived from the Mg–He,¹⁰ Ca–He,^{10–12} and Sr–He^{11,12} pair potentials are $\lambda = 2.7$, 2.1, and 2.0, respectively. Helium density functional theory (DFT) calculations of Mg

interacting with ⁴He droplets predict Mg to be bound on the surface of small droplets and delocalized in the interior of larger droplets.¹³ Experimental evidence suggests that Mg is solvated in helium droplets, both as an isolated atom¹⁴ and upon complex formation with a polar molecule.¹⁵ Since $\lambda \cong 1.9$ has been suggested as being representative of the crossover point between surface and solvated states,⁹ a Ca or Sr atom may be located in an intermediate state between the two regimes. Indeed, the helium droplet electronic absorption spectra of Ca and Sr, measured by Stienkemeier and co-workers,¹⁶ are shifted and broadened to a lesser extent than the spectra measured in bulk superfluid helium.^{17,18} However, at the same time, the solvent perturbation is larger than that observed for the surface-bound alkali atoms. The results are suggestive of a Ca and Sr location that is intermediate between a surface dimple and fully solvated state. More recent theoretical¹⁹ and experimental^{20,22} studies demonstrate that Ca and Sr are bound to the surface of ⁴He droplets in deep dimple sites,^{19–22} fully solvated in ³He droplets,^{19,22} and are located at the liquid–liquid interface of mixed ³He and ⁴He droplets.^{22–24}

In a previous study from our group, the rotational dynamics of HCN–M (M being an alkali atom) complexes were probed by vibrationally exciting the CH stretch.⁷ The HCN–M complexes have drastically modified rotational constants when compared to the constants obtained from CCSD(T) ab initio calculations. Although it is typical to measure rotational constants reduced by a factor of 2.5,² the HCN–M species have reduction factors of approximately 200. Given that the alkali atoms are known to reside on the surface of the droplet, we interpreted this large reduction in rotational constants as being due to the rotation of the HCN–M complex on the surface about

* To whom correspondence should be addressed. E-mail: douberly@uga.edu.

† University of North Carolina.

‡ Current address: Department of Chemistry University of Georgia, Athens, GA 30602.

§ Current address: NanoInk, 8025 Lamon Ave., Skokie, IL 60077.

|| Princeton University.

⊥ Current address: Max-Planck-Institut für Quantenoptik, Hans-Kopfermann-Str. 1, D-85748 Garching, Germany.

¶ University of Virginia.

the droplet center of mass. Indeed, a correlation between the size of the droplet and the magnitude of the rotational constant was clearly demonstrated.⁷ The measurement of rotational moments of inertia thus provides a spectroscopic means for determining the location of a molecular dopant, either bound on the surface or solvated within the droplet. In the present study, we investigate the location of the $(\text{HCN})_m\text{-Ca}_n$ and $(\text{HCN})_m\text{-Sr}_n$ complexes relative to the droplet surface.

Experimental Methods

The University of North Carolina helium droplet apparatus has been thoroughly reviewed² and only a brief description is given here. Helium droplets are formed by expanding ultrahigh purity helium into a vacuum through a 5 μm diameter nozzle operated between 14 and 28 K. The static pressure behind the nozzle was fixed at 60 bar. Droplet formation is a statistical process resulting in an approximately log-normal distribution of sizes with a mean and standard deviation determined from published scaling laws.²⁵ The mean droplet size is varied by changing the nozzle temperature. Changing the temperature from 14 to 28 K reduces the mean droplet size from approximately 20 000 to 1200 helium atoms. A 0.4 mm conical skimmer located 1 cm from the nozzle collimates the expansion, forming a droplet beam that passes into a second, differentially pumped chamber. The droplet beam passes through a gas pickup cell (PUC) containing HCN at approximately 2×10^{-6} Torr, and a fraction of the droplets are doped with one HCN molecule. The PUC pressure was maintained at a level to reduce the probability for formation of larger $(\text{HCN})_n$ clusters. Upon pickup, the translational and internal energy of HCN is transferred to the droplet resulting in evaporation, leading to a final temperature near 0.4 K.²⁶

The HCN–K complexes are formed upon doping the droplets with one K atom using a resistively heated copper oven as described previously.⁷ The condensation energy released upon cluster formation is rapidly removed once again by evaporative cooling.²⁷ Formation of the HCN–Ca and HCN–Sr complexes is also accomplished according to the description described before for HCN–M, M being an alkali atom.⁷ The important difference, however, is the design of the oven used to dope the droplets with the metal atoms. A 480 (450) °C temperature is required to produce the appropriate vapor pressure of Ca (Sr) necessary to maximize the droplet pickup of one atom. Both temperatures are well below the melting temperature of the bulk material, and we used an effusive metal oven introduced into the instrument through a horizontal load lock positioned either before or after the HCN gas pickup cell. The effusive oven (Dr. Karl Eberl, MBE Komponenten) consisted of a radiatively heated pyrolytic boron nitride crucible (PBN) containing either solid Ca or Sr metal. The mouth of the crucible was located about 1 cm from the droplet beam to reduce the background blackbody load on the bolometer detector. As discussed below, the experimental results are independent of the location of the oven relative to the static gas PUC containing HCN. At first, to optimize the pickup of one Ca (Sr) atom, we raised the oven temperature such that the HCN monomer CH stretch $R(0)$ signal intensity²⁸ was reduced by $\sim 40\%$, corresponding to a 480 (450) °C oven temperature. Larger $(\text{HCN})_m\text{-M}_n$ complexes are formed by increasing the pressure of HCN in the PUC or raising the temperature of the oven source.

The doped droplets pass into a third differentially pumped chamber containing a multipass cell, consisting of two parallel 15 cm long gold mirrors. Approximately 50 passes of the output of an F-center laser (Burleigh FCL-20) cross the droplet beam.

The output power and bandwidth of the laser are 10 mW and 1 MHz, respectively. The tuning and calibration of this laser are given elsewhere.²⁹ The polarization of the F-center laser is aligned parallel to a static dc Stark electric field, originating from electrodes that are positioned orthogonal to the multipass mirrors. The procedure for calibrating the Stark field is also given elsewhere.³⁰ The droplet beam flux is reduced upon resonant vibrational excitation of the $(\text{HCN})_m\text{-M}_n$ species. A bolometer detector detects this reduction in beam flux as the laser is tuned through the vibrational resonances of the molecular complex. The output from the F-center laser is amplitude modulated at 150 Hz with a mechanical chopper, and the bolometer signal is processed with a lock-in amplifier, producing background free infrared “action” spectra. The pendular state spectrum of a mixture of polar $(\text{HCN})_m\text{-M}_n$ complexes is obtained by applying an ~ 40 kV/cm Stark field to the laser interaction region.² Since the interaction energy, $\mu \cdot \mathbf{E}$, is much greater than the average rotational energy, the dipole moment of the complex is oriented parallel to the dc field. As a result, the ro-vibrational spectrum of the complex collapses into a single peak centered near the vibrational band origin.^{31,32} Individual pendular bands are assigned to a cluster size, m , by measuring the pendular transition signal intensity as the HCN pressure in the PUC is varied.²

IR–IR double resonance spectra are obtained as described in detail previously.^{33–35} Briefly, the output from a periodically poled lithium niobate optical parametric oscillator (PPLN-OPO) (Linos Photonics) is fixed in frequency and amplitude modulated at 150 Hz. The OPO frequency is resonant with the CH stretch pendular transition of either HCN–Ca or HCN–Sr. Downstream from the pump OPO, the unmodulated F-center laser is tuned through the same spectral region. The resulting IR–IR double resonance spectrum corresponds to the difference in the pendular spectrum with and without the presence of the upstream pump OPO.

Theoretical Methods

Using Molpro,³⁶ ab initio calculations for the HCN–M binary complexes were carried out at the MP2 and CCSD(T) levels of theory. Calculations for the HCN–K complex were performed at the RMP2 and RCCSD(T) levels. For all the ab initio methods, all electrons were correlated. Throughout, an aug-cc-pVTZ basis set was used for the H, C, and N atoms. For K, a 6-311++g(2d,2p) basis set was used, and relativistic, small core, effective core potentials (Stuttgart RSC ECP 1997) from the Gaussian basis set library were used for Ca and Sr.³⁷ The ECP basis sets each have 10 valence electrons with the remainder in the core. The results from the ab initio calculations are given in Table 1. The ΔI_B values correspond to the enhancement of the experimental moments of inertia relative to the CCSD(T) values. The minimum energy structures all correspond to linear complexes with the metal atom bound to the nitrogen end of HCN. The CCSD(T) counterpoise corrected²⁹ binding energies for HCN–K, –Ca, –Sr are 1026, 478, and 656 cm^{-1} , respectively. The solvation energy of a neutral impurity in a helium droplet can be calculated with DFT methods,³⁸ provided the helium–solute potentials are available. Determination of highly accurate HCN–Ca,Sr–He potential energy surfaces are, however, nontrivial and time-consuming given the high levels of ab initio theory required to accurately determine the Ca–He and Sr–He interaction energies.¹¹ An easier approach is to sum the Ca,Sr–He and HCN–He potentials^{11,39} and fit the resulting pairwise additive potential to a few high level ab initio points on the HCN–Ca,Sr–He potential. The fitted surfaces were

TABLE 1: Summary of the ab Initio and Experimental Constants for the HCN–M (M = K, Ca, Sr) Complexes

	Ab Initio Constants for HCN–M					
	MP2			CCSD(T)		
	M = Ca	M = Sr	M = K	M = Ca	M = Sr	M = K
B'' (cm ⁻¹)	0.0882	0.0667	0.0810	0.0792	0.0682	0.0809
I_B (amu Å ²)	191	253	208	213	247	208
μ_{MP2} (Debye)	6.86	6.78	6.48			
D_e (cm ⁻¹)	265	545	1025	478	656	1026
r_{N-M} (Å)	2.738	2.820	2.909	2.935	2.784	2.916

	Experimental Constants for HCN–M			
	$\bar{N} = 17\,000$		$\bar{N} = 13\,000$	
	resolved	unresolved	M = Sr	M = K
	M = Ca		M = Sr	M = K
μ'' (Debye)	6.9(1)	6.9(1)	6.9(1)	6.6(1)
μ' (Debye)	6.9(1)	7.0(1)	7.0(1)	6.7(1)
$\delta\nu$ (cm ⁻¹)	-15.70	-15.67	-15.18	-8.40
ν_0 (cm ⁻¹)	3295.50	3295.53	3296.02	3302.80
B'' (cm ⁻¹)	0.036(3)	0.00043	0.00044	0.00015
B' (cm ⁻¹)	0.036(2)	0.000431	0.00044	0.00015
D'' (cm ⁻¹)	$3(8) \times 10^{-5}$	4.8×10^{-9}	1×10^{-9}	1×10^{-9}
D' (cm ⁻¹)	$4(5) \times 10^{-5}$	4.8×10^{-9}	1×10^{-9}	1×10^{-9}
Γ (cm ⁻¹)	0.01	0.0025	0.0020	0.0020
T (K)	0.37	0.37	0.37	0.37
$B_{ab\,initio}/B_0$ v/cm	2.2	184	155	539
ΔI_0 v/cm (amu Å ²)	255	3.90×10^4	3.81×10^4	1.12×10^5
$B_{ab\,initio}/B_{510}$ v/cm	2.2	635	542	1210
ΔI_{510} v/cm (amu Å ²)	255	13.5×10^4	13.4×10^4	2.30×10^5

generated by adjusting the M–N bond length to obtain the best fit to 20 CCSD-T ab initio points on the HCN–M–He surface (aug-cc-pV5Z on He, aug-cc-pVTZ on H, C, and N, Stuttgart RSC 1997 ECP on Ca,Sr). To compare the solvation energies of the HCN–Ca,Sr species to those for the HCN–alkali atom complexes, we also produced the HCN–Na–He potential surface. The entire surface was generated at the RMP2 level of theory with an aug-cc-pVTZ basis set on all atoms. The HCN–Na complex was chosen instead of another HCN–alkali atom complex so that we could apply the largest basis set practice. Moreover, all of the HCN–alkali atom complexes exhibit the same spectral signature associated with a surface species.

For the helium density-functional calculations, the fitted potential surfaces were evaluated on a grid with spacing $\delta = 0.2376725$ Å on which the numerical calculations were performed. To minimize lattice distortions, the potentials were translated only by integer numbers of grid spacings while determining the solvation energy profiles. The helium–solute interaction potential is treated as a fixed external field for the helium atoms. This should be a good approximation for heavy solutes that move slowly compared to the helium atoms. The helium density (which we assume to be cylindrically symmetric around the linear HCN–M complexes) is varied to minimize the total energy subject to two constraints. One maintains the normalization of the helium density at a fixed number of helium atoms in the droplet. The second constrains the center of mass of the helium to a fixed point. This allows us to evaluate the solvation energy as a function of the distance ζ of the helium droplet center of mass relative to the center of mass of the HCN–M complex.

To find the helium density around an HCN–M complex, we minimize the free energy

$$\mathcal{F}[\rho] = \mathcal{E}_{\text{OTDF}}[\rho] + U_{\text{ext}}[\rho] - \mu N[\rho] - \vec{F} \cdot \vec{R}[\rho] \quad (1)$$

where $\mathcal{E}_{\text{OTDF}}[\rho]$ is the Orsay–Trento density functional³⁸ describing the ⁴He kinetic energy, interaction potential, and correlations; $U_{\text{ext}}[\rho] = \int U_{\text{ext}}(\vec{r}) \rho(\vec{r}) d^3\vec{r}$ is the He–HCN–M interaction potential (see above); $N[\rho] = \int \rho(\vec{r}) d^3\vec{r}$ is the number of helium atoms; and $\vec{R}[\rho] = N^{-1} \int \vec{r} \rho(\vec{r}) d^3\vec{r}$ is the position of the center of mass of the helium cluster. The Lagrange multiplier μ is used to fix the number of particles, and the force \vec{F} to hold the cluster center of mass at the origin of the simulation cell (in which $U_{\text{ext}}(\vec{r})$ is fixed). The distance ζ between the centers of mass of the HCN–M dopant and the helium cluster is varied by translating the He–HCN–M interaction potential $U_{\text{ext}}(\vec{r} - \zeta \vec{e}_z)$ along the symmetry axis of the simulation while keeping the cluster center of mass fixed. In our cylindrically symmetric simulations, only the axial components $Z = \vec{R} \cdot \vec{e}_z$ and $F_z = \vec{F} \cdot \vec{e}_z$ are nonzero. Once the constrained minimum of $\mathcal{F}[\rho]$ has been found, the values of these Lagrange multipliers are

$$\mu = \frac{(\vec{\nabla} \mathcal{E} \cdot \vec{\nabla} N) |\vec{\nabla} Z|^2 - (\vec{\nabla} \mathcal{E} \cdot \vec{\nabla} Z) (\vec{\nabla} N \cdot \vec{\nabla} Z)}{|\vec{\nabla} N|^2 |\vec{\nabla} Z|^2 - (\vec{\nabla} N \cdot \vec{\nabla} Z)^2} \quad (2a)$$

$$F = \frac{(\vec{\nabla} \mathcal{E} \cdot \vec{\nabla} Z) |\vec{\nabla} N|^2 - (\vec{\nabla} \mathcal{E} \cdot \vec{\nabla} N) (\vec{\nabla} N \cdot \vec{\nabla} Z)}{|\vec{\nabla} N|^2 |\vec{\nabla} Z|^2 - (\vec{\nabla} N \cdot \vec{\nabla} Z)^2} \quad (2b)$$

where $\vec{\nabla} \mathcal{E}$, $\vec{\nabla} N$, and $\vec{\nabla} Z$ are the functional gradients of the OTDF energy, the particle number, and the axial center-of-mass coordinate, respectively, with respect to the helium density; in a numerical simulation, they are the gradients of these quantities with respect to the variational parameters used to describe the helium density. For each value of the center-of-mass distance ζ the DFT simulation thus yields not only the free energy $\mathcal{F}(\zeta)$ but also the retaining force $F_z(\zeta) = -\partial \mathcal{F}(\zeta) / \partial \zeta$.

Experimental Results

HCN–K. The pendular spectrum in Figure 1 corresponds to the free CH stretch region of the linear (HCN)_m chains.⁴⁰ The potassium oven temperature was adjusted to optimize the band centered at 3302.80 cm⁻¹. The figure inset shows an expanded view of the (HCN)_m–K spectrum, which was measured with a PUC pressure adjusted to maximize the production of (HCN)₃. Each peak corresponds to a different (HCN)_m–K or (HCN)_m vibrational band, and the assignments are based on the HCN PUC pressure and K oven temperature dependence (see Supporting Information, Figures S1 and S2). The 3302.80 cm⁻¹ band is assigned to the ν_1 transition of the binary HCN–K complex and is within 0.4 cm⁻¹ of the analogous HCN–M (M = Na, Rb, Cs) CH stretch bands. An expanded, higher resolution scan of the ν_1 zero-field band is shown at the bottom of Figure 2. The spectroscopy of the binary HCN–K complex was reported previously.⁷ The zero-field HCN–K spectrum, along with the evolution of the band with Stark field strength, are shown here to illustrate the spectral signatures of a species bound to the surface of the helium droplet. As discussed in detail previously, the solute–solvent interactions are such that a linear HCN–M (M = Na, K, Rb, Cs) species resides on the surface of a helium droplet with its dipole moment pointed on average toward the droplet center.⁷ Fitting the apparent P and R contours of the

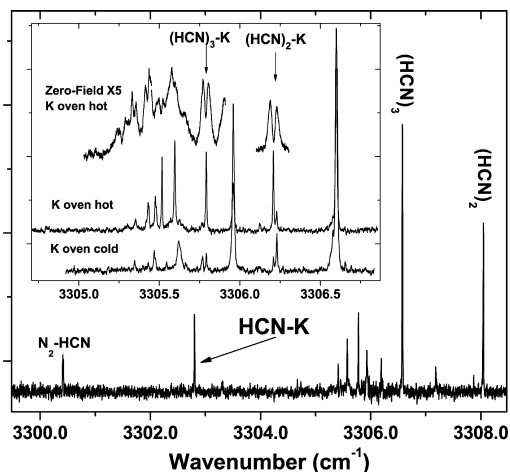


Figure 1. Pendular state spectrum of the $(\text{HCN})_m\text{-K}$ complexes. The inset shows the pendular bands for $m \geq 2$ with and without the K oven. The top curve corresponds to the zero-field spectrum.

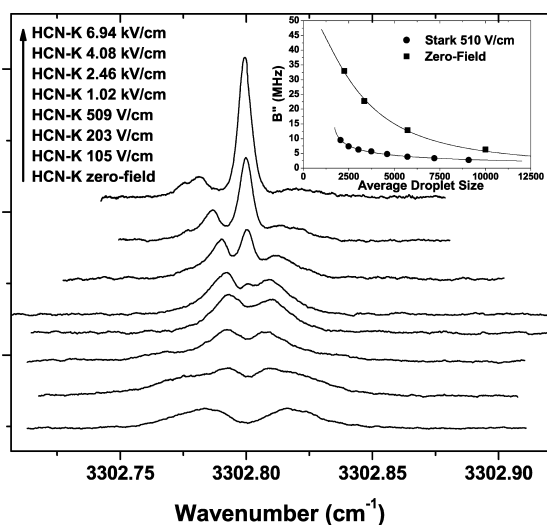


Figure 2. Evolution of the HCN-K CH stretch spectrum (3302.80 cm^{-1}) with increasing Stark field strength. The nozzle conditions were fixed at 60 bar, 19.0 K ($\bar{N} = 6000$), and the Stark field was increased as shown in the legend (increasing field from bottom to top). The inset shows the variation of B'' with average droplet size, assuming $T_{\text{rot}} = 0.37 \text{ K}$ for both the zero-field and Stark conditions. The curves through each data set are fits to the surface rotation model, $B(\bar{N}) = (5.0539 \times 10^3 \alpha) / ((M + a)[r_0(\bar{N} - b)^{1/3}]^2)$ with the following constants: for zero-field, $\alpha = 3.2(4)$, $b = 1.1(2) \times 10^3 \text{ He atoms}$; for 510 V/cm, $\alpha = 1.02(3)$, $b = 0.71(9) \times 10^3 \text{ He atoms}$. M and a are fixed to 66 and 25 amu, respectively. The rotational moment of inertia is systematically larger for the Stark (510 V/cm) spectra in comparison to the zero-field spectra, which is indicative of the temperature bias associated with the zero-field condition (see ref 7).

HCN-M zero-field spectra (which provides the product of B'' and kT_{rot}) yields rotational moments of inertia that are anomalously large in comparison to the calculated values. In addition, the moments of inertia are dependent upon the average droplet size, as shown for HCN-K in the inset of Figure 2. Both the magnitude and droplet size dependence of B'' are consistent with a model in which the HCN-M molecule rotates on the surface about the droplet center of mass.⁷ Furthermore, for a satisfactory fit to this model, the HCN-M rotational temperature must be biased with respect to the droplet temperature (0.37 K). The temperature bias ($T_{\text{rot}} \approx 1.2 \text{ K}$), observed under zero-field conditions, is apparently quenched upon application of a modest Stark field ($\sim 200 \text{ V/cm}$) to the laser interaction region. Indeed, the narrower P and R contours indicate a Stark induced reduction

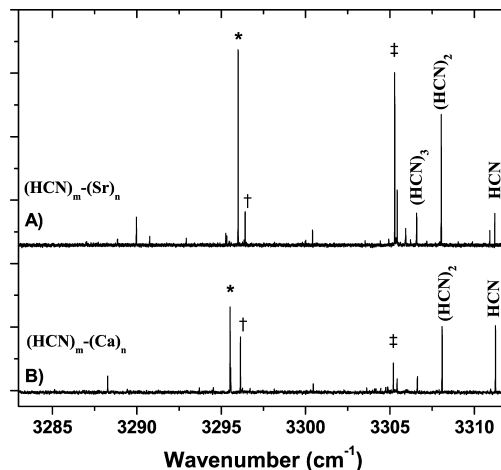


Figure 3. (A) Pendular state spectrum of the $(\text{HCN})_m\text{-(Sr)}_n$ complexes. (B) Pendular state spectrum of the $(\text{HCN})_m\text{-(Ca)}_n$ complexes. The bands labeled with an * are the CH stretch bands of the binary complexes. The † and ‡ labels are for the $\text{HCN-M}_{n \geq 2}$ and the $(\text{HCN})_2\text{-M}$ complexes, respectively.

in the product of B'' and kT_{rot} . This temperature bias for molecular dopants in helium droplets was predicted;⁴¹ however, the mechanism by which the bias is quenched by the Stark field is still undetermined. Nevertheless, these spectral signatures of a surface-bound species provide a means for differentiating between surface and solvated states of other $(\text{HCN})_m\text{-M}_n$ complexes. Also shown in the inset of Figure 1 is the zero-field spectrum of $(\text{HCN})_m\text{-K}$, $m \geq 2$, showing the surface-bound signature for the $m = 2, 3$ complexes. The evolution of the $m = 2$ band with electric field strength is given in the Supporting Information (Figure S3). The spectra for $(\text{HCN})_m\text{-M}$ ($M = \text{Na, Rb, Cs}$), $m \geq 2$, are also shown in the Supporting Information (Figure S4) and are all consistent with a surface location. Apparently, in general, the alkali atom remains on the surface as the length of the $(\text{HCN})_m$ chain increases.

HCN-Ca. The pendular spectrum shown in Figure 3B was recorded with the effusive calcium oven at $\sim 500^\circ \text{C}$. The droplet source conditions are predicted to produce an average droplet size approximately equal to 10000 He atoms. The spectrum covers the entire HCN free CH stretching region. There are several sharp peaks that can be assigned to $(\text{HCN})_m\text{-(Ca)}_n$ clusters, and the band at 3295.50 cm^{-1} (labeled with an *) is assigned to the ν_1 CH stretch band of the binary HCN-Ca complex, given the oven temperature and PUC pressure dependence of the signal. At higher oven temperatures and on average larger droplets, many new pendular bands appear that can be attributed to higher order clusters with $m, n \geq 2$, as discussed below.

We now turn our attention to the zero-field spectrum of the spectral feature near 3295.50 cm^{-1} , which is shown in Figure 4. The overall spectrum appears to be a superposition of two separate spectra. One of the two has clearly resolved rotational fine structure and a B'' rotational constant that is reduced by a factor of 2.2, when compared to the HCN-Ca ab initio value (Table 1). A reduction of this magnitude is similar to that reported for HCN-Mg and is typical for molecules solvated in helium droplets.¹⁵ As discussed previously,^{2,3} the added moment of inertia ($\sim 255 \text{ amu \AA}^2$) originates from a normal fluid component of the helium density rotating rigidly with the solvated complex.⁴²⁻⁵¹ An alternative interpretation of this same effect would be that the added moment of inertia originates from the kinetic energy of the hydrodynamic flow set up in the inhomogeneous superfluid by the rotation of the molecule.⁵²

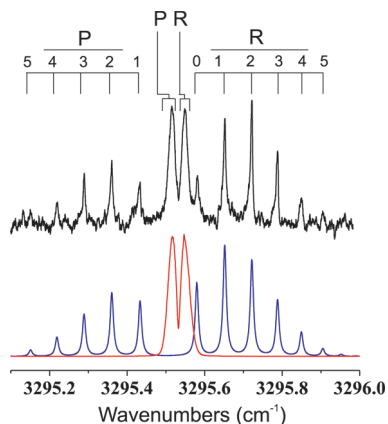


Figure 4. Zero-field spectrum of the ν_1 CH stretch band of the linear HCN–Ca complex. The nozzle conditions were fixed at 60 bar, 14.5 K ($\bar{N} = 17\,000$). The simulated spectra for the solvated (blue) and the surface-bound (red) HCN–Ca complexes are based on a linear molecule Hamiltonian.

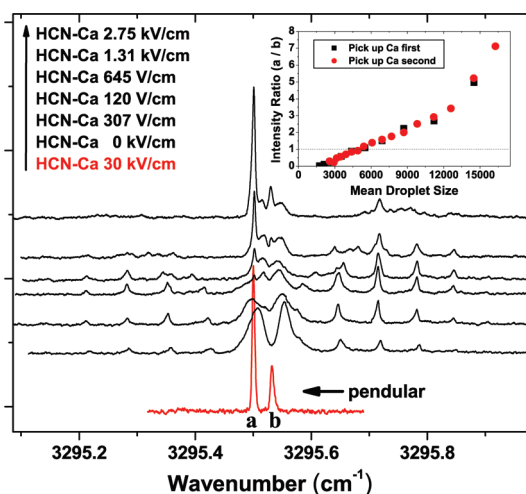


Figure 5. Evolution of the HCN–Ca CH stretch spectrum with increasing Stark field strength. The nozzle conditions were fixed at 60 bar, 18.0 K ($\bar{N} = 7200$), and the Stark field was increased as shown in the legend (increasing field from bottom to top). As the pendular regime is approached, two separate pendular peaks appear that are shifted from each other by approximately 1 GHz (bands **a** and **b**). The inset shows the variation in the intensity ratio a/b with mean droplet size, which is independent of the HCN and Ca pickup order.

The PUC pressure and oven temperature dependence of the signal along with the $B_{ab\text{ initio}}/B_{\text{He}}$ ratio provide considerable support to the assignment of the 3295.50 cm^{-1} band to the solvated HCN–Ca species. The second spectrum, shifted 1 GHz to the blue of the fully resolved band, has the same oven and pressure dependence. This spectrum exhibits the signature of a *surface-bound* complex. The width of the unresolved *P* and *R* contours is strongly correlated with the average droplet size, providing compelling evidence for an HCN–Ca surface binding site. The simulated spectra for both the solvated (blue) and surface bound (red) HCN–Ca spectra are given below the experimental spectra in Figure 4.

The evolution of the two bands with increasing Stark field is shown in Figure 5.⁵³ Satisfactory simulations of the Stark spectra are obtained with a dipole moment of 6.9(1) Debye for both the resolved and unresolved bands centered near 3295.5 cm^{-1} , providing additional support to the above assignment. Moreover, the 1 GHz blue shift of the unresolved band relative to the resolved band also supports the assignment of the former to the surface-bound species and the latter to the solvated species.

Indeed, a surface-bound species is in a distinctly different solvation environment. At the surface, less helium will contribute to the long-range attractive part of the helium–dopant potential, i.e., the part of the potential responsible for the solvent red shift. As a result, a blue shift for the surface-bound species relative to the solvated species is expected.^{54,55}

In an effort to gain insight into the origin of the two distinct HCN–Ca spectra, we monitored the relative populations of each species as a function of the droplet size. To separate the two overlapping spectra, we applied a 30 kV/cm dc field to the laser interaction region, which collapses the rotational structure of each band into a single pendular peak.^{31,32} As the Stark field increases and the pendular regime is approached, two pendular bands appear that are separated by 0.03 cm^{-1} (1 GHz). The higher frequency pendular band corresponds to the unresolved band under zero-field conditions. The population ratio of the two species is obtained by comparing the integrated intensities of the well resolved pendular bands (bands **a** and **b** in Figure 5). The inset of Figure 5 shows the integrated intensity ratio of the two HCN–Ca pendular bands measured over a wide range of source conditions ($\bar{N} = 1000\text{--}17\,000$; see Figure S5, Supporting Information). The solvated to surface-bound ratio depends strongly on the average droplet size. As the droplet size decreases, the population of solvated species diminishes while an increase is observed in the surface-bound population. As shown in Figure 5 the ratios are independent of whether Ca is picked up before or after the HCN.

The droplet size dependence of the pendular spectra suggests that there is a correlation between the average size and the dopant location. Specifically, the solvated complexes are more abundant in larger droplets, while the smaller droplets can only support the surface bound HCN–Ca complex. Given this result, we postulated that there is a droplet size threshold that determines whether the dopant resides within or on the surface of the droplet. The data in Figure 5 is consistent with a threshold around 4700 He atoms, namely the size where the intensity ratio is one to one.

The probability that a droplet of size N contains one Ca atom and one HCN molecule is defined as

$$P_{\text{occ}}(N) = P_{\text{LN}}(N) P_{\text{Ca}}(N) P_{\text{HCN}}(N)$$

where $P_{\text{LN}}(N)$ is the log-normal distribution of droplet sizes produced for a particular nozzle temperature and $P_{\text{Ca}}(N) P_{\text{HCN}}(N)$ is the probability that a droplet of size N picks up exactly one Ca atom and one HCN molecule, taking into account the helium loss that occurs after each pickup event. The HCN–Ca occupation probabilities, $P_{\text{occ}}(N)$, are determined for each source condition using a modified version of a previously reported Monte Carlo method.⁵⁶ With the $P_{\text{occ}}(N)$ distributions, we can predict the HCN–Ca solvation threshold by defining it as the value of N that satisfies the following relation for all nozzle temperatures:

$$\frac{\int_N^{\infty} P_{\text{occ}}(N') dN'}{\int_0^N P_{\text{occ}}(N') dN'} = \frac{I(\text{solv})}{I(\text{surf})} \quad (3)$$

Equation 3 is satisfied for $N = 5000 \pm 250$. The value provided by the above statistical analysis is in excellent agreement with the mean droplet size that produces the one to one pendular intensity ratio.

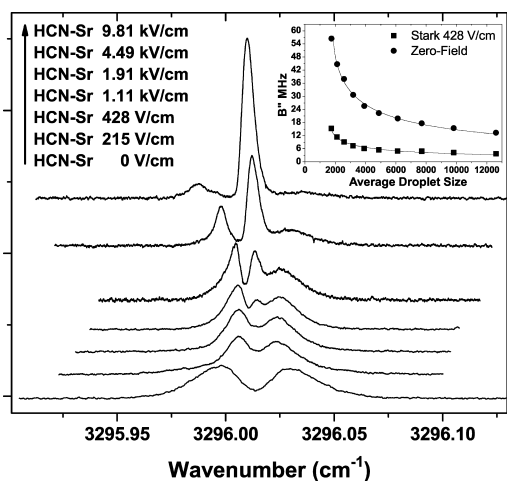


Figure 6. Evolution of the HCN–Sr CH stretch spectrum with increasing Stark field strength. The nozzle conditions were fixed at 50 bar, 16.0 K ($\bar{N} = 9700$), and the Stark field was increased as shown in the legend (increasing field from bottom to top). The inset shows the variation of B'' with average droplet size, assuming $T_{\text{rot}} = 0.37$ K for both the zero-field and Stark conditions. The curves through each data set are fits to the surface rotation model, $B(\bar{N}) = (5.0539 \times 10^5 \alpha) / ((M + a)[r_0(\bar{N} - b)^{1/3}]^2)$ with the following constants: for zero-field, $\alpha = 8.2(3)$, $b = 0.61(8) \times 10^3$ He atoms; for 428 V/cm, $\alpha = 2.0(1)$, $b = 0.8(1) \times 10^3$ He atoms. M and a are fixed to 115 and 25 amu, respectively. The rotational moment of inertia is systematically larger for the Stark (428 V/cm) spectra in comparison to the zero-field spectra, which is indicative of the temperature bias associated with the zero-field condition (see ref 7).

HCN–Sr. The pendular state spectrum of the $(\text{HCN})_m-(\text{Sr})_n$ complexes was recorded with the Sr oven temperature set to 475 °C. The most intense peak in the spectrum (3296.01 cm^{-1}), shown in Figure 3A, is assigned to the ν_1 CH stretch band of the binary HCN–Sr complex.

The assignment is again justified by the PUC pressure and oven temperature dependence of the signal intensity, along with the frequency shift from the HCN monomer, which is only 0.51 cm^{-1} less than the corresponding shift for HCN–Ca. The other intense band near 3305.2 cm^{-1} is assigned to the free CH stretch of the $(\text{HCN})_2$ –Sr linear complex. There are also other features in the spectrum that grow in intensity with increasing oven temperature and droplet size, and some of these bands, assigned to $(\text{HCN})_m-(\text{Sr})_n$ clusters, will be discussed below.

The HCN–Sr ν_1 , CH stretch spectrum is shown in Figure 6, measured at various field strengths. The zero-field and Stark spectra are characteristic of a surface-bound species, having a large effective moment of inertia that is again strongly correlated with the droplet size. Additionally, the product of B'' and kT_{rot} is reduced upon application of the Stark field. The rotational constants for both the zero field and 480 V/cm Stark spectra are plotted against the mean droplet size in the inset of Figure 6. The trends are once again consistent with the model for surface-bound rotation about an axis through the droplet center of mass.

The rotational constants and dipole moments obtained from simulations of the zero-field and Stark spectra are summarized in Table 1 ($\bar{N} = 13\,000$). The experimental dipole moment is in good agreement with the ab initio MP2 value, providing additional support to the assignment. Unlike the HCN–Ca spectrum, there is no evidence for a solvated species; that is, there is no rotationally resolved component to the HCN–Sr spectrum, regardless of the average droplet size. It is perhaps surprising that no HCN–Sr solvated population is observed,

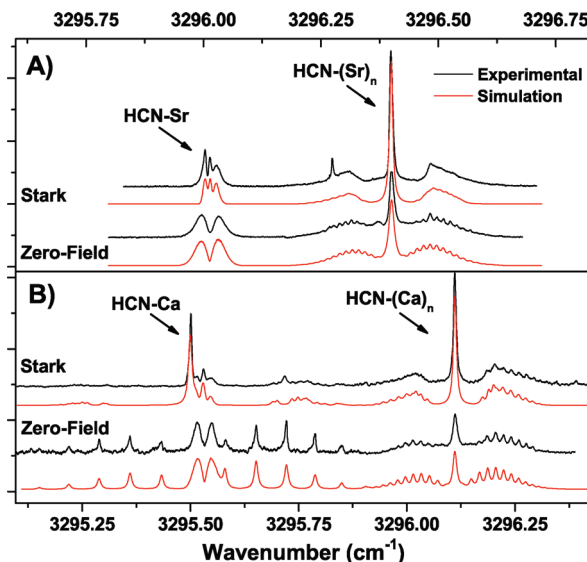


Figure 7. (A) Comparison of the simulated (red) and experimental (black) zero-field and Stark (1.92 kV/cm) spectra of the HCN– $(\text{Sr})_{n \geq 2}$ band centered at 3296.40 cm^{-1} . The zero-field spectrum was simulated using a symmetric top Hamiltonian. A dipole moment of 6.0 D was used to simulate the Stark spectrum. The spectrum of the HCN–Sr binary complex, shifted to the red (3296.01 cm^{-1}), is shown for comparison. Note the difference in the rotational constants between the binary complex and the heavier HCN– $(\text{Sr})_{n \geq 2}$ species. (B) Comparison of the simulated and experimental zero-field and Stark (1.28 kV/cm) spectra of the HCN– $(\text{Ca})_{n \geq 2}$ band centered at 3296.10 cm^{-1} . $\mu'' = 6.7$ D in the simulation. The Stark spectrum (2.75 kV/cm) of the two bands centered near 3295.5 cm^{-1} is compared to a summation (red line) of two simulated linear molecule Stark spectra. In the simulation, both μ'' dipole moments are set to 6.9 D. The agreement between the experimental and MP2 dipole moments provides additional support to the assignment of both bands near 3295.5 cm^{-1} to the HCN–Ca binary complex.

especially since the well-depths of the CCSD(T) Ca–He and Sr–He pair potentials are quite similar ($\epsilon = 3.14$ and 2.77 cm^{-1} , respectively).¹² The equilibrium M–He bond lengths at the same level of theory are 6.04 and 6.44 Å for Ca–He and Sr–He. Presumably, the subtle differences in the pair potentials are indeed important in determining the location of the complex. Perhaps, the most important factor is the equilibrium bond length, which will determine the size of the cavity produced by a solvated complex. The energetic penalty for creating the slightly larger cavity required by the HCN–Sr complex may be too large, thereby preventing HCN–Sr solvation.

Higher Order $(\text{HCN})_m-(\text{M})_n$ Clusters (M = Ca, Sr). The pendular spectra in Figure 3 have other bands that grow in intensity at higher oven temperatures. Many of these can be assigned to higher order HCN– $(\text{M})_n$ clusters by noting the oven conditions required to optimize the signal intensity of each band. For example, the intensity of the 3296.10 cm^{-1} band in Figure 3B rapidly diminishes above and below ~ 540 °C. Given the HCN PUC pressure dependence, this band can be assigned to an HCN– $\text{Ca}_{n \geq 2}$ complex. An analysis of the structures of the higher order species is given in the Supporting Information, and our intention here is to demonstrate that the larger complexes are either solvated or surface-bound on the basis of the associated spectral signature of each dopant location. Figure 7B shows the zero-field and Stark spectra of the band centered at 3296.10 cm^{-1} . The zero-field band is rotationally resolved, allowing an accurate determination of the rotational constants and dipole moment. The smooth lines in the figure are simulated zero-field and Stark (1.28 kV/cm) spectra of a symmetric top molecule with the constants reported in Table 2.

TABLE 2: Summary of the Experimental Constants Used in the Simulations of the HCN–M_{n≥2} (M = Ca, Sr) Spectra^a

	HCN–Ca _{n≥2}	HCN–Sr _{n≥2}
ν_0	3296.10	3296.40
A''	0.0398	0.0109
A'	0.0400	0.0109
B''	0.00971	0.00691
B'	0.00970	0.00692
C''	0.00971	0.00691
C'	0.00970	0.00692
D''	3.4×10^{-6}	2.3×10^{-7}
D'	3.4×10^{-6}	9.3×10^{-7}
Γ	0.008	0.013
T (K)	0.37	0.37
μ'' (D)	6.7(1)	6.0(1)
μ' (D)	6.7(1)	6.0(1)
T_{oven} (°C) ^b	541	485

^a Units are in cm^{-1} unless otherwise specified. ^b T_{oven} (°C) corresponds to the oven temperature that optimizes the pendular peak intensity, and the error bar is ± 5 °C. In comparison, the HCN–Ca and HCN–Sr bands at 3295.50 and 3296.02 cm^{-1} are optimized at 490 and 455 °C, respectively.

The rotational constants are certainly indicative of a solvated rotor. Consequently, we conclude that the formation of HCN–(Ca)_n clusters with $n \geq 2$ primarily results in solvated states. Given that we lack a probe of the bare Ca cluster, we are unable to determine if either HCN complexation leads to solvation or if the (Ca)_n cluster is solvated prior to HCN pickup. For comparison, the zero-field and Stark (2.75 kV/cm) spectra of HCN–Ca are also shown in Figure 7B. One of the authors has measured the free CH stretch of HCN–CO₂ in helium droplets, also having a pendular peak intensity at 3296.10 cm^{-1} . However, the HCN–CO₂ zero-field spectrum is considerably different than the one reported here,⁵⁷ and we are confident that we have not introduced CO₂ contamination into the beam.

Many additional bands in the (HCN)_m–(Sr)_n pendular spectrum can also be attributed to larger complexes. Moreover, both the (HCN)_m–(Sr)_n and the (HCN)_m–(Ca)_n pendular spectra have essentially the same features with most of the bands in one spectrum being shifted only by a small amount from those in the other. One of the analogous spectra is shown for the HCN–(Sr)_{n≥2} species. Figure 7A shows the zero-field and Stark (1.92 kV/cm) spectra of the pendular band centered at 3296.40 cm^{-1} . The constants used to simulate the spectra are summarized in Table 2. Also shown for comparison are the zero-field and Stark (1.92 kV/cm) spectra of the surface-bound HCN–Sr complex. The two bands were recorded with a single laser scan with oven conditions that optimized the band at 3296.40 cm^{-1} . Clearly, the HCN–Sr band is much weaker than the band to the blue at the higher oven temperature, namely 485 °C. In comparison, the intensity of the HCN–Sr band is maximized with the Sr oven at 455 °C. Comparable to the higher order HCN–(Ca)_{n≥2} spectra, the band assigned to the HCN–(Sr)_{n≥2} complex has the signature of a solvated complex; that is, the band is rotationally resolved with a moment of inertia that does not change when the external Stark field is applied. Although the binary complex is bound to the droplet surface, the complexation of an HCN molecule with a preformed (Sr)_n cluster results in a solvated dopant. Apparently, the solvated state is energetically favored upon addition of multiple Ca or Sr atoms. This is perhaps a result of the cavity surface area per metal atom being reduced, and hence the free energy penalty upon solvation, decreasing as the cluster grows.

As shown above, the (HCN)_{2,3}–K spectra are indicative of surface-bound species. Intense bands in this region are also

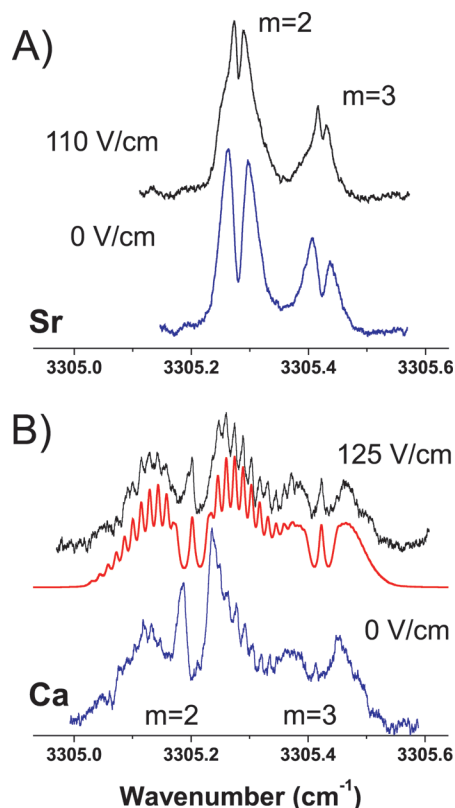


Figure 8. (A) Zero-field (blue) and Stark (110 V/cm) spectra (black) of the (HCN)_{m=2,3}–Sr complexes. Both spectra have the signature of a surface-bound species. (B) Zero-field (blue) and Stark (125 V/cm) spectra (black) of the (HCN)_{m=2,3}–Ca complexes. The red curve corresponds to a Stark simulation based on a linear molecule Hamiltonian. The B'' constant (0.0073 cm^{-1}) required to simulate the (HCN)₂–Ca spectrum gives $B_{\text{calc}}/B_{\text{exp}} = 11$, indicating a solvated species. The experimental dipole moments for the (HCN)_{m=2,3}–Ca complexes ($\mu'' = 10.5(5)$ and $20(3)$ Debye, respectively), along with the frequency shifts from (HCN)_m, support the assignment of m . Nozzle conditions were 60 bar and 18.0 K for both (A) and (B).

observed in the pendular spectra shown in Figure 3, and they are similarly assigned to (HCN)_m–Ca or (HCN)_m–Sr. The value of m is again determined from the HCN PUC pressure dependence of the pendular band intensities. Moreover, the assignment of m is supported by the trend in the “free” CH stretch red shift upon the addition of a Ca atom to the Nitrogen end of (HCN)_m. These red shifts are 15.7, 2.9, and 1.2 cm^{-1} for $m = 1, 2, 3$, respectively. An expanded, higher resolution scan of the band centered at 3305.28 cm^{-1} (Figure 3A) is shown in Figure 8A. The zero-field and Stark (110 V/cm) spectra are consistent with a surface location for (HCN)_{2,3}–Sr. In contrast, the analogous Stark spectra of the Ca species (Figure 8B) are more consistent with an interior dopant location. With a small Stark field applied (125 V/cm), the (HCN)_{2,3}–Ca spectra show rotational fine structure indicative of a solvated species. Nevertheless, the zero-field spectrum of (HCN)₂–Ca (blue trace) is not as symmetric as expected for a solvated species. As shown in the Supporting Information (Figures S6 and S7), the (HCN)₂–Ca zero-field and Stark spectra show significant droplet size dependent inhomogeneous broadening, suggesting that a fraction of these species may be surface-bound.

Photoinduced Solvation and Desolvation. Previously,³⁴ IR–IR double resonance (DR) was used to probe the photoinduced isomerization dynamics of weakly bound complexes solvated in helium droplets, due to vibrational excitation. Since two distinct populations are observed for the HCN–Ca complex,

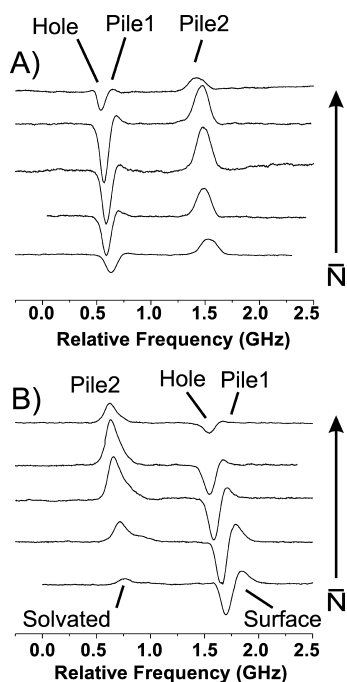


Figure 9. IR-IR DR spectroscopy of the HCN-Ca complex. The pump laser was fixed to the peak of either the (A) solvated or the (B) surface-bound species' pendular band, while the probe laser was scanned over the entire region. The droplet size range is from 3200 (bottom) to 17000 (top) helium atoms for both sets of DR spectra. The absolute cm^{-1} increases from left to right.

either solvated or surface-bound, we use IR-IR DR spectroscopy to determine the fate of one population following the absorption of the first IR photon.

Figure 9A shows the IR-IR DR spectra that correspond to pumping the solvated HCN-Ca CH stretch vibration. The DR spectra were recorded for a broad range of droplet sizes, increasing from bottom to top in the figure. The amplitude modulated upstream pump was fixed in frequency to the peak of the solvated HCN-Ca pendular band at each droplet size, and the downstream unmodulated probe laser was scanned over the entire region, resulting in a DR spectrum corresponding to the difference in the single resonance (SR) spectra with and without the pump present. The DR spectrum has three features that we can immediately assign on the basis of our previous IR-IR DR results.^{33,34} The negative DR signal (hole) corresponds to the reduction in the upstream pumped population of HCN-Ca solvated complexes. Shifted to the blue of the hole by approximately 150 MHz is a small positive DR signal (pile1) that corresponds to the upstream pumped population that remains solvated downstream after vibrational relaxation. The smaller average droplet sizes downstream lead to a slightly blue-shifted spectrum for the solvated species. Blue shifted even further from the hole (~ 1 GHz) is another positive DR signal (pile2), which is at the frequency of the surface-bound HCN-Ca pendular band.

The IR-IR DR spectra strongly support the assignment of the two bands near 3295.5 cm^{-1} to two distinct HCN-Ca populations. Furthermore, the positive DR signal (pile2) indicates that vibrational excitation of the solvated species results in a population transfer to the surface-bound species. However, it is perhaps surprising that we observe an increase in the downstream surface-bound population regardless of the initial average droplet size. One might argue that we see population transfer to the surface-bound species for all source conditions due to the droplet size distribution, having a fraction of droplet

sizes just above the solvation threshold. Recall, however, that the HCN-Ca pendular band is inhomogeneously broadened as a result of the spread in droplet sizes.³³ As a result, the upstream pump burns a hole in the inhomogeneous profile, selecting out a slice of the overall size distribution. Indeed, the width of the DR hole is only 55% as wide as the SR pendular band. Since the pump is fixed to the peak of the pendular band, we estimate that the pumped complexes reside in droplet sizes centered around the average size. Therefore, population transfer from solvated to surface states must occur in droplets well above the threshold value discussed above, given that we see significant population transfer even when $\bar{N} = 17000$ (top spectrum in Figure 9A).

Tuning the pump frequency to the peak of the surface-bound HCN-Ca pendular band, we recorded the series of DR (pump surface-bound) spectra shown in Figure 9B. Again, the DR spectra were measured over the entire dynamic range of droplet sizes. One might argue that vibrational excitation of the surface-bound species should not result in a population transfer to the solvated state, since the droplet sizes are already below the threshold presumably required for solvation. The resulting DR spectrum would then only consist of the hole and pile1 near the frequency of the pump, being simply due to the overall reduction of the droplet size. However, pumping the surface-bound species *does* result in DR signals (pile2) for the solvated complex. Surprisingly, vibrational excitation of the surface-bound species enhances the downstream solvated population, regardless of the initial droplet size.

Since vibrational excitation of surface-bound HCN-Ca leads to an enhanced solvated population, we also recorded the analogous DR spectra for HCN-Sr. The SR pendular and DR spectra of the HCN-Sr band are shown for a range of droplet sizes in Figure 10A,B, respectively. Once again, in contrast to HCN-Ca, there is only one band observed for HCN-Sr, even for the largest average droplet sizes ($\bar{N} = 17000$). As shown in Figure 6, the B'' constant is strongly correlated with the droplet size and is significantly reduced from its ab initio value, indicating that HCN-Sr resides on the surface of the helium droplet. The DR spectra, given in Figure 10B, show a positive DR signal (pile2) shifted to the red of the negative DR (hole) by ~ 750 MHz. The frequency shift is similar to the 1 GHz shift observed between the solvated and surface-bound HCN-Ca spectra. Therefore, we assign the new positive peak observed in the DR spectrum to the solvated HCN-Sr species. The HCN-Sr DR spectrum proves unequivocally that vibrational excitation of the surface-bound species ultimately leads to a solvated complex. Interestingly, the relaxation channel leading to solvation is completely closed for the smaller average droplet sizes. Increasing the nozzle temperature from 13.5 K (top DR spectrum) to 18.0 K (bottom DR spectrum) decreases and broadens the positive DR signal until it completely disappears. Population transfer to the solvated state is apparently precluded below average droplet sizes around 8000 helium atoms, whereas HCN-Ca population transfer was observed for all source conditions.

Discussion

We begin this section with a brief review of the HCN-Ca and HCN-Sr spectroscopic results. Reminiscent of the HCN-M spectra, where M is an alkali atom, the HCN-Sr CH stretch band has the signature of a species bound to the surface of the helium droplet. HCN-Ca similarly has this signature, yet there is a second band that can be assigned to a bulk-solvated HCN-Ca species. Above, we have rationalized this observation

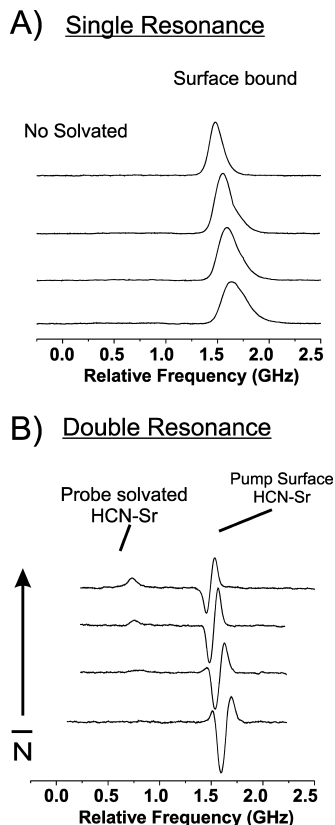


Figure 10. (A) SR pendular spectra of the HCN–Sr complex at several average droplet sizes, increasing from bottom to top with a range of approximately 6000–17000 helium atoms. (B) IR–IR DR spectroscopy of the HCN–Sr complex. The pump laser was fixed to the peak of the only pendular band present in the SR spectrum ($\sim 3296.01 \text{ cm}^{-1}$), while the probe laser was scanned over the same region. The average droplet sizes are the same as in (A), increasing from bottom to top. The absolute cm^{-1} increases from left to right.

in terms of two distinct HCN–Ca populations, either *surface-bound* or *solvated*. Each HCN–Ca complex is apparently trapped in one of the two states following cluster formation within (or on) the droplet. Furthermore, the relative abundance of the two states strongly depends on the initial size of the helium droplet yet is independent of the dopant pickup order; the solvated species is favored in larger droplets, and the surface species is more abundant in droplets with less than about 5000 helium atoms. IR–IR DR shows definitively that vibrational excitation of the CH stretch will either solvate or desolvate the HCN–Ca molecular complex. Moreover, the double resonance spectra demonstrate the relation between the two bands assigned to HCN–Ca. Surprisingly, we also found that vibrational excitation will *solvate* surface-bound HCN–Sr, although this is only observed for droplets larger than $\sim \bar{N} = 8000$.

The vibrational excitation induced population transfer observed here is reminiscent of our earlier work on the vibrational induced isomerization dynamics of hydrogen bonded complexes within helium droplets.^{34,35} For example, a similar IR–IR DR scheme was employed to study the isomerization between two stable configurations on the HCN–HF potential energy surface.³⁴ Excitation of either the CH or HF stretch fundamental is sufficient to induce a population transfer between the bent HF–HCN and linear HCN–HF isomers. In this example, the barrier between the two isomers is low in comparison to the vibrationally excited state energy. It is reasonable to consider a similar explanation for the two distinct HCN–Ca species, along with the observed photoinduced solvation and desolvation. If a

solvation barrier exists on the droplet-solute free energy surface, then a condensing HCN–Ca species could become delocalized over surface and solvated states. Relaxation of the HCN–Ca condensation energy could then result in a distribution of species trapped on either side of the barrier. Additionally, if the barrier is smaller than $\sim 3000 \text{ cm}^{-1}$, CH stretch excitation and subsequent vibrational relaxation may lead to a redistribution between surface and solvated states. Formation of solvated HCN–Sr complexes may be precluded because of a relatively larger solvation barrier, originating from the less attractive Sr–He pair potential, in comparison to Ca–He. Indeed, the experimental results are consistent with these proposals.

To test these ideas, we carried out helium density functional calculations to determine the solvation energy of the HCN–M ($M = \text{Na}, \text{Ca}, \text{Sr}$) species as a function of its axial position (ζ) relative to the droplet center of mass. As an example, Figure 11 shows the density profile of an HCN–Na complex solvated at its minimum-energy position in a smaller droplet ($N = 2000$). We can see a competition between the solvation-shell structure of quasi-adsorbed helium atoms onto the heliophilic hydrogen end of the complex, and the buoyancy potential of the relatively large and repulsive alkali atom. The present calculation is for a specific complex, but we believe the qualitative result of a surface-bound species should apply to most complexes of a single heliophile with an alkali atom or other strong heliophobe. The reason, simply, is that the force driving most heliophiles toward the center of the droplet is quite weak once the heliophile is solvated with one layer of helium. For this case, the endothermic cost of solvating the Na atom can be avoided if the HCN heliophile is solvated near the surface with its dipole moment oriented on average toward the droplet center of mass. The buoyancy effect of M can be quantified by calculating the effective number of helium atoms displaced by a fully solvated HCN–M complex.⁵⁸ Inside droplets of $N = 4000$ with $\zeta = 0$, we estimate these at 4.3 ($M = \text{Na}$), 2.5 (Ca), and 3.0 (Sr) ⁴He atoms.

Figure 12 gives the calculated solvation energies of HCN–M ($M = \text{Na}, \text{Ca}, \text{Sr}$) as a function of ζ for an $N = 4000$ droplet. The HCN–Na complex is clearly surface-bound, with an energy of 65 cm^{-1} necessary for bulk solvation. This energy is not available in a helium nanodroplet at $T = 0.37 \text{ K}$, which supports the assignment of the spectroscopy results⁷ to a surface-bound complex. Unfortunately, with our current DFT code we cannot calculate the energy associated with bending the complex relative to the local surface normal, as that would remove the assumed cylindrical symmetry. However, it is clear that the solvation energy change upon 180° rotation is vastly higher than the rotational constant for bare HCN–Na (0.13 cm^{-1}), and thus we expect the complex to be strongly aligned along the axis connecting the HCN–Na and droplet centers of mass. Thus, the dipole correlation function of HCN–Na will reflect not rotation of the complex around its own center of mass but the translational motion of the complex around the periphery of the helium nanodroplet.

For the HCN–Ca complex, the DFT calculations only predict a fully bulk-solvated state, and there is no free energy minimum at the droplet surface. This is in contrast to the experimental results showing both a surface-bound and a solvated species. For HCN–Sr, the DFT calculations predict *both* surface-bound and bulk-solvated states. The two states are almost iso-energetic (within 0.05 cm^{-1}) and are separated by a barrier of 2.2 cm^{-1} . Again this does not match the experimental results of purely surface-bound states. However, in experiments there may be a

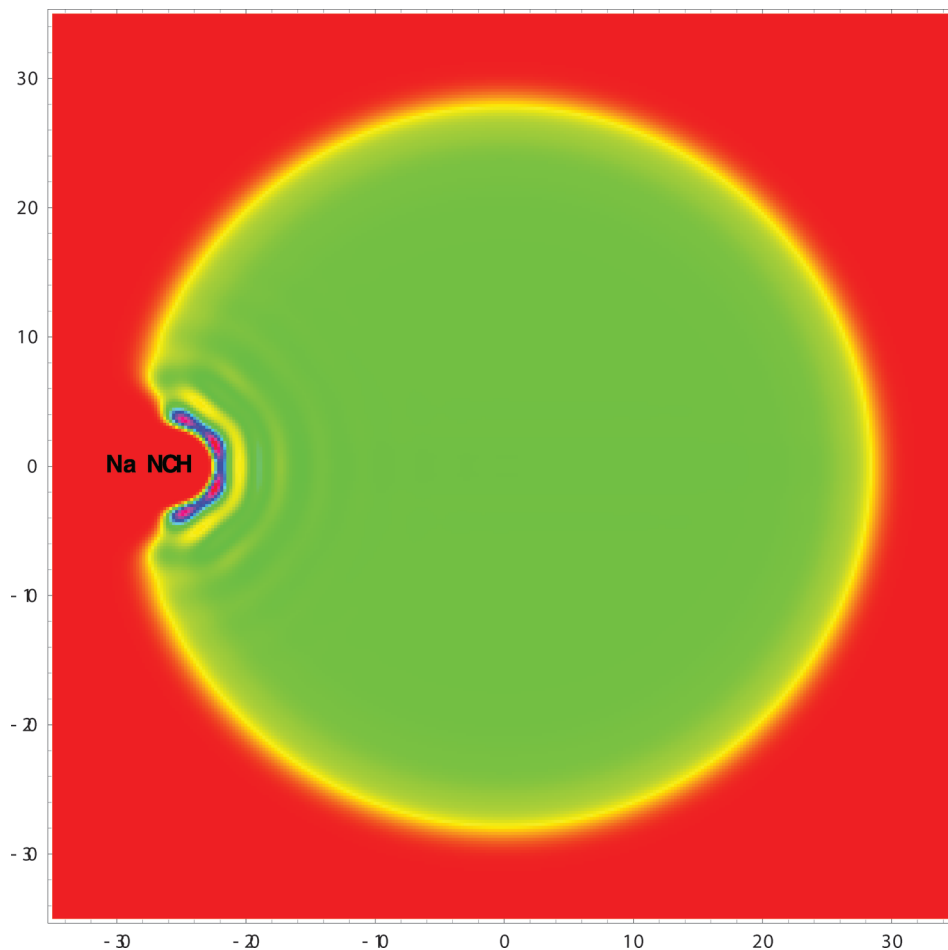


Figure 11. Helium profile around a surface-solvated HCN–Na molecule. The centers of the chemical symbols correspond to the equilibrium positions of the dopant atoms. The droplet contains $N = 2000$ helium atoms. Distances are given in Å.

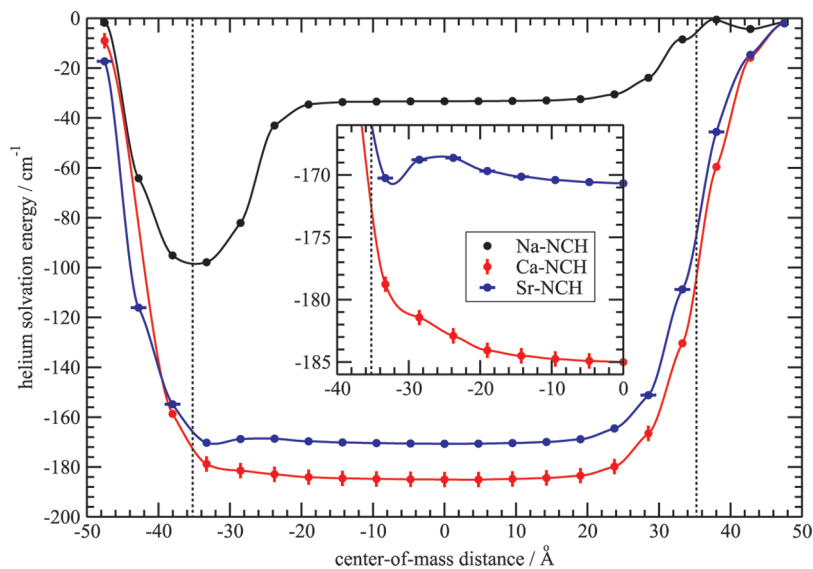


Figure 12. Effective solvation energies $\mathcal{F}(\xi)$ of HCN–M complexes ($M = \text{Na}, \text{Ca}, \text{Sr}$) with axis perpendicular to a helium nanodroplet of size $N = 4000$, as a function of center-of-mass distance. The continuous lines are cubic interpolations taking the derivatives $\partial\mathcal{F}/\partial\xi$ from eq 3 into account. The inset shows a closeup of the HCN–Sr solvation barrier. Dotted lines mark the liquid-drop model radius $R_{\text{dm}} = 35.2$ Å.

centrifugal bias toward surface state population, not taken into account in zero-temperature DFT calculations.

For the HCN–M ($M = \text{Na}, \text{K}, \text{Rb}, \text{Cs}$) droplet size dependent rotational constant to fit a simple surface rotation model, we had to assume a rotational temperature of ~ 1.3 K,⁷ although the droplet temperature is known from previous experiments

to be close to 0.37 K. Nevertheless, due to the conservation of angular momentum, microcanonical equilibrium between the droplet and the rotor leads to a rotor temperature which does not match that of the droplet.^{41,59} For molecules previously considered, this effect is small because the root mean squared (rms) angular momentum of the rotor is much less than that of

the droplet. In the case of HCN–M complexes, this is no longer true and the effects of the bias could be quite large. A quantitative calculation of this effect would require knowledge of the helium droplet angular momentum distribution, which we unfortunately do not know. Qualitatively, it is clear that rotation of the HCN–M complex around the droplet surface is the lowest energy excitation to store trapped angular momentum as long as the angular velocity is less than that of the lowest droplet ripplon. The significant temperature bias required to fit the surface rotation model⁷ suggests that the rms angular momentum of the complex is much larger than that of the same rotor if one assumes canonical equilibrium. Furthermore, this may result in a significant centrifugal potential biasing the effective potentials of Figure 12 toward surface-bound states. The HCN–Ca angular momentum required to produce a metastable surface state can be estimated from the potential in Figure 12. At the droplet surface, the force pulling the HCN–Ca complex toward the center is about $4 \text{ cm}^{-1} \text{ \AA}^{-1}$. For a counteracting inertial force ($J^2/\mu R^3$) of this magnitude, an HCN–Ca angular momentum of $J \sim 600\hbar$ is required. This value of J can be compared to the mean angular momentum transferred to the droplet upon Ca or Sr capture; that is, $1500\hbar$ and $2000\hbar$, respectively.

The helium DFT results support our initial interpretation. Given the qualitative differences in the barrier heights on the HCN–Ca and HCN–Sr solvation potentials, it is reasonable to suspect that the lack of a solvated HCN–Sr complex and the mixture of HCN–Ca states is due to a comparatively larger HCN–Sr solvation barrier (including the centrifugal effects). The lack of solvated HCN–Sr states also suggests that cluster formation occurs close to the surface where the complex is subsequently trapped behind the solvation barrier. One possible mechanism for the photoinduced solvation of surface bound HCN–Ca or HCN–Sr involves the transfer of vibrational energy to translational energy, such that the surface-bound species can sample the solvated potential minimum. It is well-known that the relaxation of a vibrationally excited complex results in the evaporation of several hundred helium atoms. This evaporative cooling may effectively reduce the solvation barrier by reducing the contribution from centrifugal effects, originating from the angular momentum trapped in HCN–M surface rotation. Either of these mechanisms, or a combination of the two, are consistent with the observed population shift to solvated complexes following CH stretch excitation of the surface species. However, for HCN–Ca, we see both photoinduced solvation *and* desolvation, suggesting that the barrier between the two states survives the evaporation process, given that a fraction of the downstream complexes are surface-bound following vibrational excitation of the solvated species. Further theoretical work will be required to shed light on the size dependent ratio of surface to solvated HCN–Ca states, and the droplet size threshold for the observation of photoinduced HCN–Sr solvation; both of these observations are at least suggestive of a droplet size dependent solvation barrier, which apparently decreases for larger droplet sizes.

Summary

HCN–M (M = K, Ca, Sr) complexes were formed on the surface of helium nanodroplets, and the rotational dynamics were probed with IR laser spectroscopy. For the HCN–Sr CH stretch band, the spectral signature of a surface-bound complex is observed, reminiscent of the ν_1 ro-vibrational bands of the HCN–M complexes, where M is a Na, K, Rb, or Cs atom.⁷ Solvation necessarily requires a cavity to form in the liquid

around the solute, which results in an increase in the free energy. If the free energy decrease due to the attractive solute–solvent interaction does not compensate for this increase, then the solute will remain near the droplet surface. Apparently, the energetic penalty is too large for HCN–Sr solvation to occur, in analogy to the HCN–alkali atom complexes. For the HCN–Ca complex, the ν_1 spectrum is characteristic of a superposition of solvated and surface-bound species. Two vibrational bands are observed, one with rotational fine structure and the other with the surface-bound signature, that is, an unresolved *P* and *R* contour with a droplet size dependent rotational constant. The two band origins are separated by 1 GHz, and the relative intensities of the two are droplet size dependent, with the rotationally resolved band dominating in the larger droplets. Presumably, the interaction between the HCN–Ca solute and the helium solvent is favorable enough such that solvation can occur; although, we are observing the transition regime, where a fraction of the complex formation events do not lead to solvation. The *solvated* HCN–Ca is 7 times more abundant than the *surface-bound* species when droplets with $\bar{N} = 17\,500$ are used. IR–IR double resonance spectroscopy proves unequivocally that the two bands separated by 1 GHz are due to two separate HCN–Ca populations, which we assign to solvated and surface-bound states. Vibrational excitation of one HCN–Ca population results in a transfer to the other, independent of the average droplet size. Surprisingly, although the single resonance results show that the surface-bound population is favored in the smaller droplets, the vibrational excitation induced solvation of the surface-bound species is observed in even the smaller average droplet sizes, namely $\bar{N} = 3200$. As noted above, only a surface-bound population is observed in the single resonance spectroscopy of HCN–Sr. Nevertheless, the complex is solvated upon vibrationally exciting the CH stretch (3296.01 cm^{-1}), although this is only observed with $\bar{N} \gtrsim 8000$ helium atoms.

Helium density functional calculations for HCN–M (M = Na, Ca, Sr) show a strongly surface-bound state for M = Na, purely solvated state for M = Ca, and both surface and solvated states separated by a 2.2 cm^{-1} barrier for M = Sr. However, due to centrifugal effects, the solvation barriers will be larger than those predicted by the zero temperature DFT calculations. Angular momentum deposited into the droplet upon dopant pickup may subsequently be trapped in the surface rotation of the HCN–M complex, leading to a centrifugal bias toward surface-bound complexes. The qualitative difference in the DFT HCN–Ca and HCN–Sr solvation barriers is consistent with (i) the lack of solvated HCN–Sr complexes in the experimental IR spectra and (ii) the observed mixture of surface and solvated HCN–Ca complexes.

We also measured the rotational constants and dipole moments of several HCN–(M)_{n≥2} complexes. The moments of inertia are significantly smaller than those measured for the lighter HCN–M surface-bound species, suggesting that the solvated state is energetically favored upon the further addition of metal atoms to the complex. Apparently, as the cluster grows, the free energy penalty upon solvation per metal atom decreases, resulting in a solvated cluster.

Acknowledgment. This work was supported by the National Science Foundation (R.E.M., Grant No. CHE-99-87740; K.K.L., Grant No. CHE-0700740). G.E.D. acknowledges the Graduate School at UNC-CH for a Royster Fellowship and Professor Michael A. Duncan and the NSF (Duncan, Grant No. CHE-0551202) for additional support.

Supporting Information Available: Figures showing HCN pickup cell pressure dependence of the $(\text{HCN})_m$ -K spectra (Figure S1), frequency red shift of the $(\text{HCN})_m$ “free” CH stretch band (Figure S2), evolution of the $(\text{HCN})_2$ -K “free” CH stretch band with electric field (Figure S3), pendular and zero-field spectra of $(\text{HCN})_{2,3}$ -Na,Cs (Figure S4), droplet size dependence of the two pendular bands associated with HCN-Ca (Figure S5), Stark spectra of $(\text{HCN})_2$ -Ca (Figure S6), evolution of the $(\text{HCN})_2$ -Ca zero-field spectrum with increasing droplet size (Figure S7), Stark spectra of $(\text{HCN})_2$ -Sr (Figure S8), zero-field and Stark spectra of HCN-Ca_{n≥2} (Figures S9 and S10). Tables of experimental constants used to simulate the HCN-M_n spectra (Table S1) and ab initio constants obtained for the HCN-(Ca)_n complexes (Table S2). This material is available free of charge via the Internet at <http://pubs.acs.org>.

References and Notes

- Toennies, J. P.; Vilesov, A. F. *Angew. Chem., Int. Ed.* **2004**, *43*, 2622–2648.
- Choi, M. Y.; Doublerly, G. E.; Falconer, T. M.; Lewis, W. K.; Lindsay, C. M.; Merritt, J. M.; Stiles, P. L.; Miller, R. E. *Int. Rev. Phys. Chem.* **2006**, *25*, 15–75.
- Barranco, M.; Guardiola, R.; Hernández, S.; Mayol, R.; Navarro, J.; Pí, M. *J. Low Temp. Phys.* **2006**, *142*, 1–81.
- Stienkemeier, F.; Lehmann, K. K. *J. Phys. B: At. Mol. Opt. Phys.* **2006**, *39*, 127–166.
- Küpper, J.; Merritt, J. M. *Int. Rev. Phys. Chem.* **2007**, *26*, 249–287.
- Lugovoj, E.; Toennies, J. P.; Vilesov, A. F. *J. Chem. Phys.* **2000**, *112*, 8217–8220.
- Doublerly, G. E.; Miller, R. E. *J. Phys. Chem. A* **2007**, *111*, 7292–7302.
- Stienkemeier, F.; Vilesov, A. F. *J. Chem. Phys.* **2001**, *115*, 10119–10137.
- Ancilotto, F.; Lerner, P. B.; Cole, M. W. *J. Low Temp. Phys.* **1995**, *101*, 1123–1146.
- Hinde, R. J. *J. Phys. B, At. Mol. Opt. Phys.* **2003**, *36*, 3119–3128.
- Lovallo, C. C.; Klobukowski, M. *J. Chem. Phys.* **2004**, *120*, 246–252.
- Lovallo, C. C.; Klobukowski, M. *Chem. Phys. Lett.* **2003**, *373*, 439–447.
- Hernando, A.; Barranco, M.; Mayol, R.; Pí, M.; Krosnicki, M. *Phys. Rev. B* **2008**, *77*, 024513.
- Reho, J.; Merker, U.; Radcliff, M. R.; Lehmann, K. K.; Scoles, G. *J. Chem. Phys.* **2000**, *112*, 8409–8416.
- Stiles, P. L.; Moore, D. T.; Miller, R. E. *J. Chem. Phys.* **2003**, *118*, 7873–7881.
- Stienkemeier, F.; Meier, F.; Lutz, H. O. *J. Chem. Phys.* **1997**, *107*, 10816–10818.
- Bauer, H.; Beau, M.; Friedl, B.; Marchand, C.; Miltner, K.; Reyher, H. *J. Phys. Lett. A* **1990**, *146*, 134.
- Gunther, H.; zu Putlitz, G.; Tabbert, B. *Z. Phys. B* **1995**, *98* (special issue).
- Mateo, D.; Barranco, M.; Mayol, R.; Pí, M. *Eur. Phys. J. D* **2009**, *52*, 63–66.
- Hernando, A.; Mayol, R.; Pí, M.; Barranco, M.; Ancilotto, F.; Bunermann, O.; Stienkemeier, F. *J. Phys. Chem. A* **2007**, *111*, 7303–7308.
- Hernando, A.; Barranco, M.; Mayol, R.; Pí, M.; Ancilotto, F. *Phys. Rev. B* **2008**, *78*, 184515.
- Bunermann, O.; Dvorak, M.; Stienkemeier, F.; Hernando, A.; Mayol, R.; Pí, M.; Barranco, M.; Ancilotto, F. *Phys. Rev. B* **2009**, *79*, 214511.
- Przystawik, A.; Gode, S.; Doppner, T.; Tiggesbaumker, J.; Meiwes-Broer, K. H. *Phys. Rev. A* **2008**, *78*, 021202(R).
- Ren, Y.; Kresin, V. V. *Phys. Rev. A* **2007**, *76*, 043204.
- Knuth, E. L.; Schilling, B.; Toennies, J. P. in *International Symposium on Rarefied Gas Dynamics*; Oxford University Press: United Kingdom, 1995; Vol. 19, pp 270–276.
- Hartmann, M.; Miller, R. E.; Toennies, J. P.; Vilesov, A. F. *Phys. Rev. Lett.* **1995**, *75*, 1566–1569.
- Brink, D. M.; Stringari, S. *Z. Phys. D* **1990**, *15*, 257–263.
- Nauta, K.; Miller, R. E. *Phys. Rev. Lett.* **1999**, *82*, 4480–4483.
- Huang, Z. S.; Jucks, K. W.; Miller, R. E. *J. Chem. Phys.* **1986**, *85*, 3338–3341.
- Doublerly, G. E.; Miller, R. E. *J. Phys. Chem. B* **2003**, *107*, 4500–4507.
- Rost, J. M.; Griffin, J. C.; Friedrich, B.; Herschbach, D. R. *Phys. Rev. Lett.* **1992**, *68*, 1299–1301.
- Block, P. A.; Bohac, E. J.; Miller, R. E. *Phys. Rev. Lett.* **1992**, *68*, 1303–1306.
- Merritt, J. M.; Doublerly, G. E.; Miller, R. E. *J. Chem. Phys.* **2004**, *121*, 1309–1316.
- Doublerly, G. E.; Merritt, J. M.; Miller, R. E. *Phys. Chem. Chem. Phys.* **2005**, *7*, 463–468.
- Doublerly, G. E.; Merritt, J. M.; Miller, R. E. *J. Phys. Chem. A* **2007**, *111*, 7282–7291.
- Werner, H. J.; Knowles, P. J.; Amos, R. D.; Bernhardsson, A.; Berning, A.; Celani, P.; Cooper, D. L.; Deegan, M. J. O.; Dobbyn, A. J.; Eckert, F.; Hampel, C.; Hetzer, G.; Korona, T.; Lindh, R.; Lloyd, A. W.; McNicholas, S. J.; Manby, F. R.; Meyer, W.; Mura, M. E.; Nicklass, A.; Palmieri, P.; Pitzer, R.; Rauhut, G.; Schutz, M.; Schumann, U.; Stoll, H.; Stone, A. J.; Tarroni, R.; Thorsteinsson, T. *MOLPRO*, version 2002.1; 2002.
- Kaupp, M.; Schleyer, P. v. R.; Stoll, H.; Preuss, H. *J. Chem. Phys.* **1991**, *94*, 1360–1366.
- Dalfovo, F.; Lastrì, A.; Pricapenko, L.; Stringari, S.; Treiner, J. *Phys. Rev. B* **1995**, *52*, 1193–1209.
- Atkins, K. M.; Hutson, J. M. *J. Chem. Phys.* **1996**, *105*, 440–450.
- Nauta, K.; Miller, R. E. *Science* **1999**, *283*, 1895–1897.
- Lehmann, K. K. *J. Chem. Phys.* **2004**, *120*, 513–515.
- Paesani, F.; Viel, A.; Gianturco, F. A.; Whaley, K. B. *Phys. Rev. Lett.* **2003**, *90*, 73401.
- Paesani, F.; Whaley, K. B. *J. Chem. Phys.* **2004**, *121*, 4180–4192.
- Paesani, F.; Whaley, K. B. *J. Chem. Phys.* **2004**, *121*, 5293–5311.
- Moroni, S.; Blinov, N.; Roy, P. N. *J. Chem. Phys.* **2004**, *121*, 3577–3581.
- Paesani, F.; Kwon, Y.; Whaley, K. B. *Phys. Rev. Lett.* **2005**, *94*, 153401.
- Moroni, S.; Sarsa, A.; Fantoni, S.; Schmidt, K. E.; Baroni, S. *Phys. Rev. Lett.* **2003**, *90*, 143401.
- Paolini, S.; Fantoni, S.; Moroni, S.; Baroni, S. *J. Chem. Phys.* **2005**, *123*, 114306.
- Tang, J.; McKellar, A. R. W.; Mezzacapo, F.; Moroni, S. *Phys. Rev. Lett.* **2004**, *92*, 145503.
- Xu, Y.; Blinov, N.; Jager, W.; Roy, P. *J. Chem. Phys.* **2004**, *124*, 081101.
- Moroni, S.; Blinov, N.; Roy, P. *J. Chem. Phys.* **2004**, *121*, 3577–3581.
- Callegari, C.; Conjusteau, A.; Reinhard, I.; Lehmann, K. K.; Scoles, G.; Dalfovo, F. *Phys. Rev. Lett.* **1999**, *83*, 5058–5061.
- The unresolved component of the zero-field spectrum in Figure 5 is slightly broader and more intense than the one shown in Figure 4. This is consistent with the Figure 5 spectra being recorded under conditions that produced a smaller average droplet size. See Figure 4 and 5 captions.
- Lehmann, K. K. *Mol. Phys.* **1999**, *97*, 645–666.
- Callegari, C.; Lehmann, K. K.; Schmied, R.; Scoles, G. *J. Chem. Phys.* **2001**, *115*, 10090–10110.
- Lewerenz, M.; Schilling, B.; Toennies, J. P. *J. Chem. Phys.* **1995**, *102*, 8191–8207.
- Doublerly, G. E. *Infrared Laser Spectroscopy of Dopants In and On Helium Nanodroplets: Rotational and Vibrational Dynamics*, Ph.D. thesis, The University of North Carolina at Chapel Hill: Chapel Hill, NC, 2006.
- Lehmann, K. K.; Northby, J. A. *Mol. Phys.* **1999**, *97*, 639–644.
- Lehmann, K. K.; Dokter, A. M. *Phys. Rev. Lett.* **2004**, *92*, 173401.